Journal of Hydrology 444–445 (2012) 146–160

Contents lists available at SciVerse ScienceDirect

Journal of Hydrology

journal homepage: www.elsevier.com/locate/jhydrol

Catchment-scale reconstruction of glacier mass balance using observations and global climate data: Case study of the Hailuogou catchment, south-eastern Tibetan Plateau

Yong Zhang [a,b,*], Yukiko Hirabayashi [a], Shiyin Liu [b]

[a] Institute of Engineering Innovation, The University of Tokyo, 2-11-16 Yayoi, Bunkyo-ku, Tokyo 113-0032, Japan
[b] State Key Laboratory of Cryospheric Sciences, Cold & Arid Regions Environmental & Engineering Research Institute, Chinese Academy of Sciences, Lanzhou 730000, China

ARTICLE INFO

Article history:
Received 7 September 2011
Received in revised form 2 April 2012
Accepted 8 April 2012
Available online 17 April 2012
This manuscript was handled by
Konstantine P. Georgakakos, Editor-in-Chief

Keywords:
Glacier
Mass balance
Debris cover
Catchment scale
Tibetan Plateau

SUMMARY

Debris-covered glaciers are common in the Tibetan Plateau, where ablation zones are mantled in a supraglacial debris cover that influences glacier mass balance, runoff, and response to climate change by affecting the melt rate of the underlying ice. The impact of debris cover has not yet been taken into account in regional- or global-scale assessments of glacier mass balances and freshwater resources by using physically based numerical models. Here, a surface energy–mass balance model that accounts for the significance of debris cover and its effect on the ice melt rate is applied to reconstruct the glacier mass balance of Hailuogou catchment, which is located in the south-eastern Tibetan Plateau and contains three debris-covered and four debris-free monsoonal maritime glaciers. According to our calculations, the glaciers in Hailuogou catchment show a mean annual balance of −0.42 m water equivalent (w.e.) per year, for a total mass loss of 24.3 m w.e. over the period 1952–2009. A comparison of summer temperature- and precipitation-mass balance/equilibrium line altitude (ELA) relations indicates that the glaciers in the catchment are much more sensitive to temperature change than to precipitation change. In the last 20 yrs, increasing summer temperature is the main cause of rapid wasting of the glacier mass in the catchment. Meanwhile, the presence of supraglacial debris markedly accelerates glacier mass loss, resulting in the unstable termini of debris-covered glaciers in Hailuogou catchment. This highlights the importance of debris cover for understanding glacier mass balance and hydrology in the Tibetan Plateau.

1. Introduction

Mountain glaciers are a vital source of water in many of the world's river basins (Lemke et al., 2007) as well as sensitive indicators of climate change (Oerlemans and Fortuin, 1992). Glacier mass balance (mass gain or loss at the surface over a certain time period) forms a vital link between climate change and glacier dynamics and hydrology, and its monitoring is the best way to infer climate change from glaciers. The Tibetan Plateau and surrounding mountain ranges contain massive glaciers with a total area of 116,180 km^2, whereas mass balance measurements have been made on only 40 glaciers at one time or another since 1946 (Dyurgerov and Meier, 2005). Most regional mass balance estimates for the Tibetan Plateau glaciers are based on extrapolation of only about 40 mostly short duration (<5 yrs in most cases) and unevenly distributed surface mass balance records (Dyurgerov and Meier, 2005; Ohmura, 2006; Lemke et al., 2007) covering less than 1% of the total glacier area. Furthermore, the Tibetan Plateau contains a large number of debris-covered glaciers. In these cases, ablation zones are mantled in a supraglacial debris cover that influences glacier melt rates (Nakawo and Young, 1982; Mattson et al., 1993; Mihalcea et al., 2006; Zhang et al., 2011) and terminus dynamics (Scherler et al., 2011), which can modify a glacier's response to climate change. Although several numerical models have been proposed for calculating the insulating effect of debris cover on different glaciers (e.g. Nakawo and Young, 1982; Fukushima et al., 1987; Braun et al., 1993; Nicholson and Benn, 2006; Reid and Brock, 2010; Zhang et al., 2011; Immerzeel et al., 2012), so far no physically based numerical mass-balance models have been developed on a large spatial unit (e.g. on a catchment scale) that can consider the significance of debris cover and its influence on ice melt rates that have determined glacier mass balances. We argue that the estimates reported in previous studies (e.g. Dyurgerov and Meier, 2005; Ohmura, 2006; Lemke et al., 2007) lead to substantial uncertainty in the mass loss from the Tibetan Plateau, especially in regions where debris-covered glaciers exist. Hence, there is an urgent need for better methods, which can consider the significance of debris cover and its impact on the ice melt rate, to quantify mass changes from the Tibetan Plateau glaciers.

* Corresponding author at: Institute of Engineering Innovation, The University of Tokyo, 2-11-16 Yayoi, Bunkyo-ku, Tokyo 113-0032, Japan. Tel.: +81 3 5841 0717.
E-mail address: zhyong@sogo.t.u-tokyo.ac.jp (Y. Zhang).

0022-1694/$ - see front matter © 2012 Elsevier B.V. All rights reserved.
http://dx.doi.org/10.1016/j.jhydrol.2012.04.014

In recent years, physically based mass balance models have been applied to individual glaciers driven using in situ meteorological observations (e.g. Arnold et al., 1996; Fujita and Ageta, 2000; Klok and Oerlemans, 2002; Hock and Holmgren, 2005; Sakai et al., 2009). However, the application of these models to large spatial units (e.g. on a catchment scale) has been limited because of the inadequate spatial and temporal coverage of local meteorological records and mass balance observations (Barry, 2006). To overcome this problem, climate model simulations have been used. A few studies have investigated the ability of climate model simulations to drive energy balance models (e.g. Reichert et al., 2001; Bougamont et al., 2005; Hock et al., 2007; Fujita et al., 2011; Fujita and Nuimura, 2011), and degree-day models (e.g. Hock et al., 2007; Hirabayashi et al., 2010) for modeling mass balance. Their results indicate that climate model simulations provide an opportunity to be used for reconstructing mass balance over a long period in the regions that are not routinely monitored.

In this study, we implement a surface energy–mass balance modeling approach that takes into account the significance of debris cover and its impact on the ice melt rate, to reconstruct the glacier mass balance of Hailuogou catchment in the south-eastern Tibetan Plateau, forcing the model by observations and global climate data. Hailuogou catchment is chosen as the best case because it offers an opportunity to study a monsoonal maritime glacier system with debris-covered and debris-free glaciers in the south-eastern Tibetan Plateau, where specific, though incomplete, information is available about both glaciology and meteorology. The main aim of this study is to present a simple, physically-based approach considering the significance of debris cover and its influence to estimate as accurately as possible the long-term variation and trend in surface mass balance on a catchment scale. By this approach, the effect of supraglacial debris cover on glacier mass balance can be assessed. This, in turn, allows us to document ongoing glacier and climate changes in the south-eastern Tibetan Plateau, one of the largest and most sensitive remaining areas of temperate ice (Li and Su, 1996), covering approximately the same area as the Southern Patagonia Icefield (Rignot et al., 2003). Specifically, we validate the global climate data in the Hailuogou catchment and explore the potential to use global climate products for mass balance modeling of glaciers on the Tibetan Plateau, where the harsh climatic conditions and remoteness hamper ground-based monitoring and result in very poor data coverage.

2. Study area

Hailuogou catchment (80.5 km^2) is located on the eastern slope of Mount Gongga, south-eastern Tibetan Plateau (29.6°N, 101.9°E) (Fig. 1). The catchment contains seven glaciers covering an area of 36.44 km^2 (Table 1) (Pu, 1994). These seven glaciers are named from Glacier No. 1 to Glacier No. 7 in Fig. 1. Hereafter, the largest glacier (No. 3) is called Hailuogou Glacier. Among the seven glaciers, the ablation zones of Glacier No. 1, No. 2, and Hailuogou Glacier are covered by supraglacial debris cover supplied from mixed ice/snow/rock avalanches occurring on the icefall and the surrounding walls through frost weathering processes and structural rockfalls (Li and Su, 1996). In situ debris thickness surveys on Hailuogou Glacier indicated that the debris thickness increases from just several millimetres of patchy cover below ~3650 m above sea level (a.s.l.) to >1 m at the glacier terminus (Zhang et al., 2011).

The catchment climate is characterized by the southeast monsoon in summer and westerly circulation in winter (Li and Su, 1996). The mean annual air temperature (1988–2004) observed at the Gongga Alpine Ecosystem Observation and Research Station (hereafter, GAEORS; 3000 m a.s.l.; Fig. 1) is 4.1 °C, and mean annual precipitation (1988–2004) is 1906 mm w.e. Summer precipitation (May–October) accounts for ~80% of the annual total.

Glaciers in the catchment have retreated considerably since the early 20th century (Table 1) (Su et al., 1992; Liu et al., 2010; Zhang et al., 2010). The total glacier area of the catchment decreased by 2.9 km^2 over the period 1966–2007, representing 7.8% of the total glacier area in 1966 (Liu et al., 2010). Zhang et al. (2010) noted that the ablation area of Hailuogou Glacier thinned by -1.1 ± 0.4 m yr^{-1} during the period 1966–2009, and the thinning has accelerated significantly since 1989. The termini of Glacier No. 2 and Hailuogou Glacier retreated by ~1100 m during the period 1930–1990 (Su et al., 1992) and ~1878 m during the period 1930–2007 (Su et al., 1992; Liu et al., 2010), respectively.

3. Data

We use various datasets, including meteorological observations at GAEORS, daily global gridded data of temperature and precipitation from the closest grid of the catchment, runoff records from GAEORS, ablation data from Hailuogou Glacier, glacier area data, debris thickness data, and a digital elevation model (DEM) with a resolution of 30 m. These datasets are briefly described below.

3.1. Meteorological data

GAEORS (Fig. 1) has been operated near the terminus of Hailuogou Glacier since 1988. Daily temperature, wind speed, relative humidity, and precipitation data are available at GAEORS for the period 1988–2009. An automatic weather station (AWS; Fig. 1) was installed in the ablation area of Hailuogou Glacier at ~3550 m a.s.l. in April 2008. Air temperature, relative humidity, wind speed, and the incoming and reflected solar radiation are recorded at 10-min intervals. Precipitation has been measured by a precipitation gauge installed at the margin of Hailuogou Glacier (3500 m a.s.l.; Fig. 1) since April 2008, and its 30-min average was stored. All variables were compiled to daily values.

To reconstruct the long-term glacier mass balance variation in Hailuogou catchment, a global 0.5° gridded dataset of near-surface temperature and daily precipitation for 57 yrs from 1951 to 2007 is used. The temperature dataset was generated by Hirabayashi et al. (2008) based on monthly temperature values of the Climate Research Unit version TS 2.1 data set for the period 1951–2002 (CRU; Mitchell and Jones, 2005), and the dataset of Fan and van den Dool (2008) for the period 2003–2007 (hereafter, H08). Full details of the H08 dataset and generation methods have been reported by Hirabayashi et al. (2008). The daily precipitation dataset for 1951–2007 was created by collecting rain gauge observation data across Asia (Yatagai et al., 2009). This is the only long-term continental-scale daily product that contains a dense network of daily rain gauge data for Asia including the Himalayas and mountainous areas in the Middle East (Yatagai et al., 2009) (hereafter, Y09). Full details of the Y09 dataset can be found in the work of Yatagai et al. (2009) or at http://www.chikyu.ac.jp/precip/index.html. The altitude information of each grid cell is derived from an SRTM digital elevation model (February 2000; Jarvis et al., 2008).

3.2. Runoff and area data

Runoff derived from the catchment has been measured at the river outlet of the catchment located at the terminus of Hailuogou Glacier since 1994 (Fig. 1). Records are available for the period 1994–2002. In this study, monthly runoff observations are used as simulation targets to calibrate and verify the energy–mass balance model.

The area of each glacier in the catchment derived from the Chinese Glacier Inventory (Pu, 1994) is shown in Table 1, representing the area information before 1966. To estimate the glacier area in

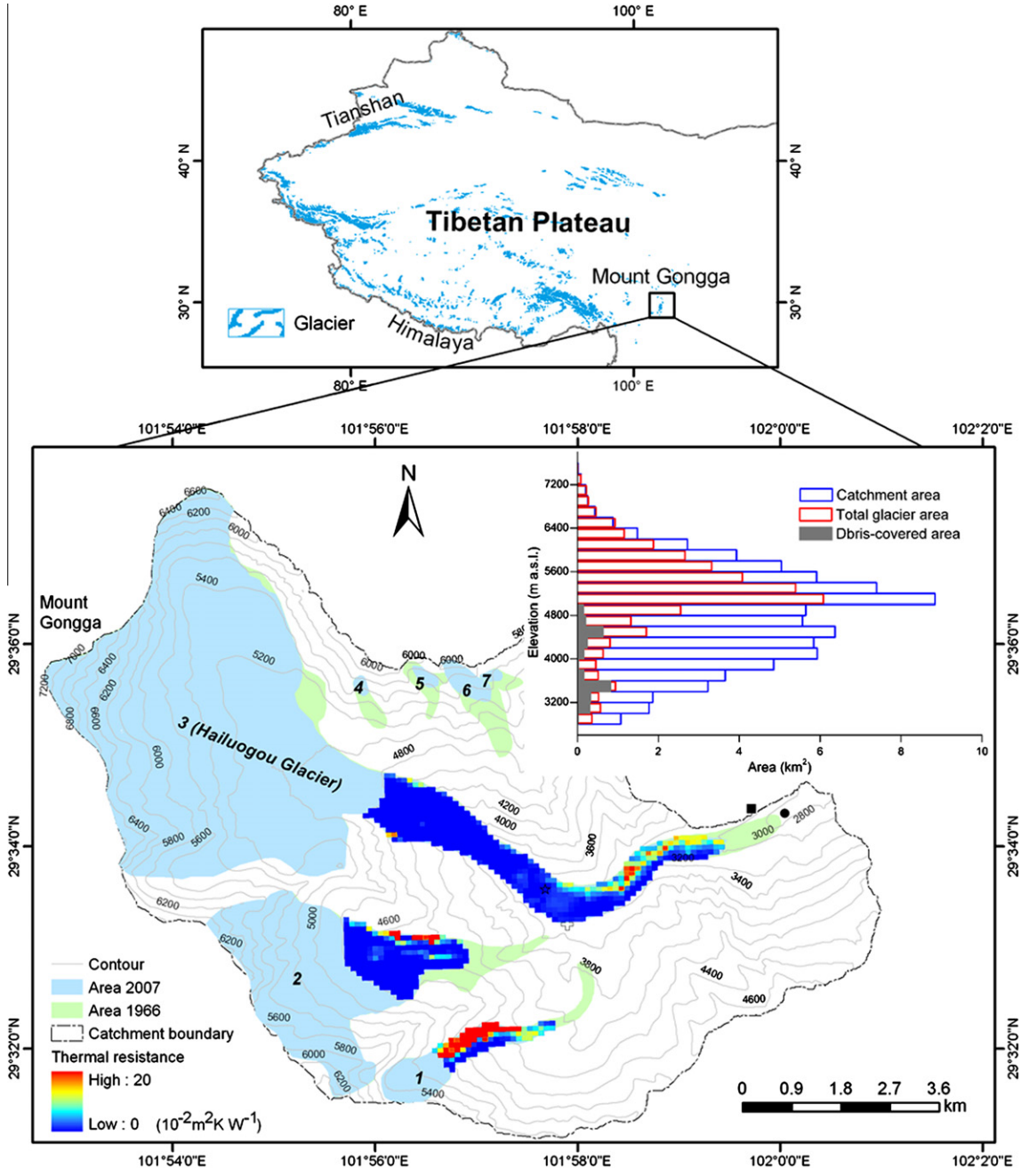

Fig. 1. Map of Hailuogou catchment on the eastern side of Mount Gongga in the south-eastern Tibetan Plateau, spatial distribution of thermal resistance of the debris layer and area-altitude distributions of the catchment, glacier, and debris-covered surface. GAEORS denotes the Gongga Alpine Ecosystem Observation and Research Station (square). AWS denotes the automatic weather station (star). The circle marks the hydrological station for runoff observation. The cross is the precipitation gauge. Glacier boundaries in 1966 and 2007 are derived from Liu et al. (2010). Spatial distribution of thermal resistance of the debris layer is derived from Zhang et al. (2011). The histogram shows the area-altitude distributions of the debris-covered ice (gray), the glaciers (red), and the catchment (blue). (For interpretation of the references to color in this figure legend, the reader is referred to the web version of this article.).

Table 1
Characteristics of seven glaciers in Hailuogou catchment. Glacier area, length and elevation are derived from the Chinese Glacier Inventory (Pu, 1994). Annual variation rate (AVR) of glacier area is derived from Liu et al. (2010).

Glacier	Elevation (m a.s.l.)	Length (km)	Area (km^2)	AVR (% yr^{-1})	Debris-covered
No. 1	3740–5400	4.3	1.44	0.38	Yes
No. 2	3600–6368	5.6	7.67	0.21	Yes
No. 3	2990–7556	13.1	25.71	0.09	Yes
No. 4	5120–5840	0.9	0.33	1.80	No
No. 5	5080–6000	1.1	0.37	1.68	No
No. 6	4720–6136	2.0	0.66	1.45	No
No. 7	5280–5800	0.8	0.26	1.52	No

different periods, glacier outlines in 1966, 1975, 1994, and 2007 are used. These were created by Liu et al. (2010) based on topographic maps and remote sensing data. Full details of these data can be found in the work of Liu et al. (2010).

3.3. Mass balance data

The first ablation measurement in the catchment was performed on the ablation area of Hailuogou Glacier in 1982 with 23 stakes (Li and Su, 1996). Since then, ablation measurements have been conducted discontinuously at a network of ablation stakes distributed over the ablation area of Hailuogou Glacier (Liu et al., 1994; Su et al., 1996; Zhang et al., 2011). Ablation data in 1982/83 (Li and Su, 1996), 1990/91–1993/94 (Liu et al., 1994; Su et al., 1996), and 2008 (Zhang et al., 2011) are used to verify the performance of the energy–mass balance model.

Snow depth was measured at 150 points across an altitudinal range of 4900–5500 m a.s.l. in October 1990 (Aizen and Aizen, 1994; Liu et al., 1994). A mean snow density of 415 kg m^{-3} was obtained from five snow pits and a crevasse with distinct annual layer in the accumulation area of Hailuogou Glacier (Aizen and Aizen, 1994; Liu et al., 1994). This snow density is used to convert all snow-related mass balance measurements into water equivalent.

3.4. Debris thickness data

The first debris thickness surveys in the catchment were carried out on Hailuogou Glacier in 1982 at 23 points across an altitudinal range of 2960–3600 m a.s.l. (Li and Su, 1996). In 2009, extensive in situ surveys of debris thickness were conducted at 300 points on Hailuogou Glacier, and these points were surveyed across the entire ablation area in the altitudinal range of 2900–3600 m a.s.l. (Zhang et al., 2011).

Data of thermal resistances of debris layers are used to map the spatial distribution of debris cover in the catchment (Fig. 1) and calculate the ice melt rate beneath the debris. The thermal resistance of the debris layer is defined as debris thickness divided by the thermal conductivity of the debris layer (Nakawo and Young, 1981, 1982). Field determinations of the thickness and thermal conductivity of the debris layer are especially time-consuming and not practical on glaciers. Zhang et al. (2011) calculated thermal resistance of debris layers from the surface temperature derived from the thermal infrared bands of ASTER and the net radiation estimated from the visible/near-infrared bands of ASTER and NCEP/NCAR reanalysis data that corresponded to the nearest time and location of ASTER acquisition. An analysis of the transverse and longitudinal profiles of the ground-surveyed debris thicknesses and ASTER-derived thermal resistances of debris layers indicated that the ground-surveyed debris thicknesses and ASTER-derived thermal resistances of debris layers correlate strongly over the entire ablation area, and across- and along-glacier patterns of ASTER-derived thermal resistance correspond well with spatial patterns of debris thickness, which can reflect large-scale variations in the extent and thickness of the debris cover (Zhang et al., 2011). Full details of the thermal resistance of the debris cover and its calculation method can be found in the work of Zhang et al. (2011).

3.5. Digital elevation model

A DEM of the catchment was produced from aerial photographs acquired in 1989 (Zhang et al., 2010). The accuracy of the DEM was validated by the global positioning system (GPS) data on glacier-free terrain, yielding a root mean square error (RMSE) of 11.2 m (Zhang et al., 2010). We use the DEM to spatially distribute meteorological data and compute the area of each elevation band in the catchment.

4. Methods

4.1. Catchment discretization

Hailuogou catchment is divided, at intervals of 50 m, into a set of elevation bands based on the DEM. Each elevation band is assumed to have a homogenous hydrological behavior. The areas of each elevation band in 1966, 1975, 1994, and 2007, which are used to calculate the area-averaged mass balance, are obtained from the DEM based on glacier outlines for 1966, 1975, 1994, and 2007. The area-altitude distributions of the glacier and the catchment are shown in Fig. 1. Although shrinkage of the glaciers was reported in the catchment (e.g. Su et al., 1992; Liu et al., 2010; Zhang et al., 2010), glacier altitude-area distributions in 1966, 1975, 1994, and 2007 are correspondingly supposed to be constant for the periods 1952–1966, 1967–1975, 1976–1994 and 1995–2009.

Ablation zones of Glacier No. 1, Glacier No. 2, and Hailuogou Glacier are subdivided into debris-covered and debris-free surfaces. This separation is completely based on the spatial distribution of the thermal resistance of the debris layer (Fig. 1). The thermal resistance of the debris layer can be used to be as a proxy for the debris thickness over large areas because the thermal resistance of the debris layer correlates strongly with the ground-surveyed debris thickness, the spatial pattern of which reflects large-scale variations in the extent and thickness of the debris cover (Zhang et al., 2011). The area-altitude distribution of debris-covered surfaces is shown in Fig. 1.

4.2. Meteorological data pre-processing

For each elevation band, the temperature and precipitation time series are interpolated according to the mean elevation. The air temperature is assumed to decrease with increasing altitude with a constant lapse rate. Cao and Cheng (1994) estimated the temperature lapse rate at Mount Gongga as -4.3 °C km^{-1} on the eastern slope and -5.4 °C km^{-1} on the western slope. Here, the lapse rate is fixed to -4.3 °C km^{-1}. This rate is confirmed by recent observations at GAEORS and the AWS in the ablation area of Hailuogou Glacier.

Precipitation increases linearly with altitude in this region (Aizen and Aizen, 1994; Cao and Cheng, 1994; Cheng, 1996; Liu et al., 2010). We apply a precipitation gradient d_{prec} (% of precipitation increase per meter of elevation increase) from the snout to the top of the glacier. Thus, the precipitation, P, at each elevation band is calculated as

$$P = P_{\mathrm{GAEORS}}[1 + d_{prec}(h - h_{\mathrm{GAEORS}})], \quad (1)$$

where P_{GAEORS} is precipitation at GAEORS, and h and h_{GAEORS} are the altitudes of the elevation band and GAEORS, respectively. Based on results of previous studies (Aizen and Aizen, 1994; Cao and Cheng, 1994; Liu et al., 1994, 2010; Cheng, 1996), we estimate the daily orographic precipitation gradients of this region varying between 12% and 60% per 100 m. However, precipitation has spatial variability in the glacierized regions of high mountainous catchments. Accurate spatial interpolation of precipitation data series is therefore difficult to obtain and the prevailing extreme conditions imply significant measurement uncertainty. In particular, the value of the precipitation gradient is difficult to estimate in the accumulation zones of the catchment, where precipitation data are scarce. This difficulty in the spatial interpolation of precipitation is a significant source of modeling uncertainty for glacier mass balance and runoff simulations. Considering this, here we treat the precipitation gradient as a tunable model parameter.

In addition, because wind speed only weakly correlates with the melt rate (Ohmura, 2001), and has a little influence on the mass

balance results (Fujita and Ageta, 2000; Sakai et al., 2009; Fujita et al., 2011), wind speed observed from GAEORS is not interpolated and assumed representative for the entire area calculated.

4.3. Global climate data validation and bias correction

Air temperature and precipitation observed from GAEORS are used to validate the global climate data (H08 and Y09). A linear regression analysis is used to determine the correlation between the global climate data and observed variables on daily, monthly, seasonal and annual timescales. The H08 temperature is validated for the period 1988–2007 using data from GAEORS, and the Y09 precipitation is validated for the period 1988–2004. After evaluating the association between the two datasets, we correct the global climate data for model bias on a daily timescale by a linear regression method because the global climate data are frequently biased relative to in situ observations due to their parameterization schemes and coarse grid resolution. Linear regression equations are established between in situ meteorological observations and global climate data over the period 1988–1997. These are expressed as follows:

$$T_{\mathrm{GAEORS}} = 0.995T_{H08} - 2.559 \quad (r = 0.88; p < 0.001; \ \mathrm{RMSE} = 2.7\ ^{\circ}\mathrm{C}), \tag{2}$$

$$P_{\mathrm{GAEORS}} = 1.250P_{\mathrm{Y09}} + 2.199 \quad (r = 0.71; p < 0.001; \ RMSE = 0.003\ \mathrm{m}), \tag{3}$$

where T_{GAEORS} and P_{GAEORS} are daily temperature and precipitation at GAEORS, respectively, and T_{H08} and P_{Y09} are H08 temperature and Y09 precipitation, respectively.

4.4. Surface energy–mass balance model

The surface energy–mass balance model consists of two coupled components. The first is to compute the energy available for melting from energy exchange between the debris-covered/free surface and the atmosphere, and accumulation. The second is to treat processes occurring in the subsurface after meltwater percolates in the underlying layers (Fig. 2). The model calculates the surface mass balance for each elevation band at a time step of one day. The annual mass balance for each elevation band ($i = 1...n$), b_i, is calculated as

$$b_i = \sum_{t=t_0}^{t_1} [Ca(t) + M(t) + R_F(t)], \tag{4}$$

where M represents ablation (mass loss is defined negatively), Ca (positive sign) is accumulation (snow), and R_F (positive sign) is refreezing. All terms are in units of m w.e. t_0 is the start date of the mass balance year (here, 1 October), and t_1 is the end date of the mass balance year (30 September in the following year). The annual mass balance of the entire catchment, B, is estimated as the area-weighted sum of the mass balance in all elevation bands, which is calculated as

$$B = \frac{\sum_{i=1}^{n} b_i S_i}{\sum_{i=1}^{n} S_i}, \tag{5}$$

where S_i is the discrete value of the surface area for each elevation band ($i = 1...n$) (m^2).

The glacier melt, M, in the ith elevation band is computed using a surface energy-balance model. For the debris-free ice, the energy available for melting, Q_M, is calculated from

$$Q_M = (1 - \alpha)R_S + R_{Ld} + R_{Lu} + Q_S + Q_L + Q_R + Q_G, \tag{6}$$

where R_S and R_{Ld} are the downward short- and long-wave radiation fluxes, respectively, R_{Lu} is the upward long-wave radiation flux, Q_S, Q_L, Q_R and Q_G are the net sensible heat flux, net latent heat flux, heat flux by rain on the surface and conductive heat flux into the glacier surface, respectively, and α is the surface albedo. All terms are taken to be positive toward the surface, in units of $\mathrm{W\,m^{-2}}$. Zhang et al. (2011) analyzed the effect of Q_R on ice melt rates on Hailuogou Glacier, and found that it was not significant. Hence, the heat flux by rain is not taken into account. Downward long-wave radiation is obtained from the air temperature, relative humidity and ratio of downward short-wave radiation to that at the top of the atmosphere using an empirical scheme (Fujita and Ageta, 2000). The upward long-wave radiation is calculated from the Stefan–Boltzmann constant and the surface temperature assuming a black body for the snow/ice surface, and turbulent sensible- and latent-heat fluxes were calculated using the bulk method. They are expressed as follows

$$\begin{aligned} R_{Lu} &= \varepsilon\sigma(T_S + 273.2)^4 \\ Q_S &= c_a\rho_a CU(T_a - T_S) \\ Q_L &= l_e\rho_a CU[rhq(T_a) - q(T_S)], \end{aligned} \tag{7}$$

where σ is the Stefan–Boltzmann constant ($5.67 \times 10^{-8}\ \mathrm{W\,m^{-2}\,K^{-4}}$), ε is the emissivity of the glacier surface (taken to be 1), T_S is the surface temperature (°C), T_a is the air temperature (°C), c_a is the specific heat capacity of air ($1006\ \mathrm{J\,kg^{-1}\,K^{-1}}$), ρ_a is the density of air ($\mathrm{kg\,m^{-3}}$), C is the bulk coefficient for sensible and latent heat (0.002), U is the wind speed ($\mathrm{m\,s^{-1}}$), l_e is the latent heat of the evaporation of water ($2.5 \times 10^6\ \mathrm{J\,kg^{-1}}$), q is the saturated specific humidity ($\mathrm{kg\,kg^{-1}}$) calculated as a function of air temperature using the empirical equations presented by Kondo (1994), and rh is the relative humidity. Before 1988, relative humidity data were not available in the catchment. Fig. 3a shows the relation between the monthly means of precipitation and relative humidity established based on observations at the AWS during the period October 2008–July 2009. The relation indicates relative humidity increasing with precipitation and is used to estimate the daily relative humidity from the daily precipitation. As shown in Fig. 3b, the estimated relative humidity is in agreement with the observed data for the period May–September 2008.

The absorbed short-wave radiation is calculated from the surface albedo and downward short-wave radiation. The surface albedo calculation in the model follows the albedo scheme of Fujita (2007). This method was applied to different regions and validated against observations (e.g. Sakai et al., 2009; Fujita et al., 2011; Fujita and Nuimura, 2011; Yasunari et al., 2011). In their studies, the albedo is calculated by a simplified concept of multiple scattering in the ice plate whose thickness is related to the surface snow density. The albedo, α, in the Fujita (2007) scheme is given by

$$\alpha = r_I + \frac{(1 - r_I)^2\tau}{1 - r_I\tau}, \tag{8}$$

where

$$\tau = \frac{(1-T_I) - \sqrt{(1-T_I)^2 - R_I^2}}{R_I}$$

$$T_I = \frac{(1-r_I)^2 \exp(-k_I l_I)}{1 - r_I^2 \exp(-2k_I l_I)}$$

$$R_I = r_I + \frac{(1-r_I)^2 r_I \exp(-2k_I l_I)}{1 - r_I^2 \exp(-2k_I l_I)}$$

In these equations r_I is the reflectivity of ice (0.018), R_I is the reflectance of a single ice plate, T_I is the transparency of a single ice plate, l_I is the effective ice thickness, and k_I is the absorption coefficient of ice (assumed to be $10\ \mathrm{m^{-1}}$). The effective ice thickness l_I can be determined from

$$l_I = \frac{2}{\rho_i S^*}, \tag{9}$$

where ρ_i is the density of ice (assumed to be $900\ \mathrm{kg\,m^{-3}}$), and S^* ($\mathrm{m^2\,kg^{-1}}$) represents specific surface area (the area of the surface of the ice particles in unit mass of snow), computed with

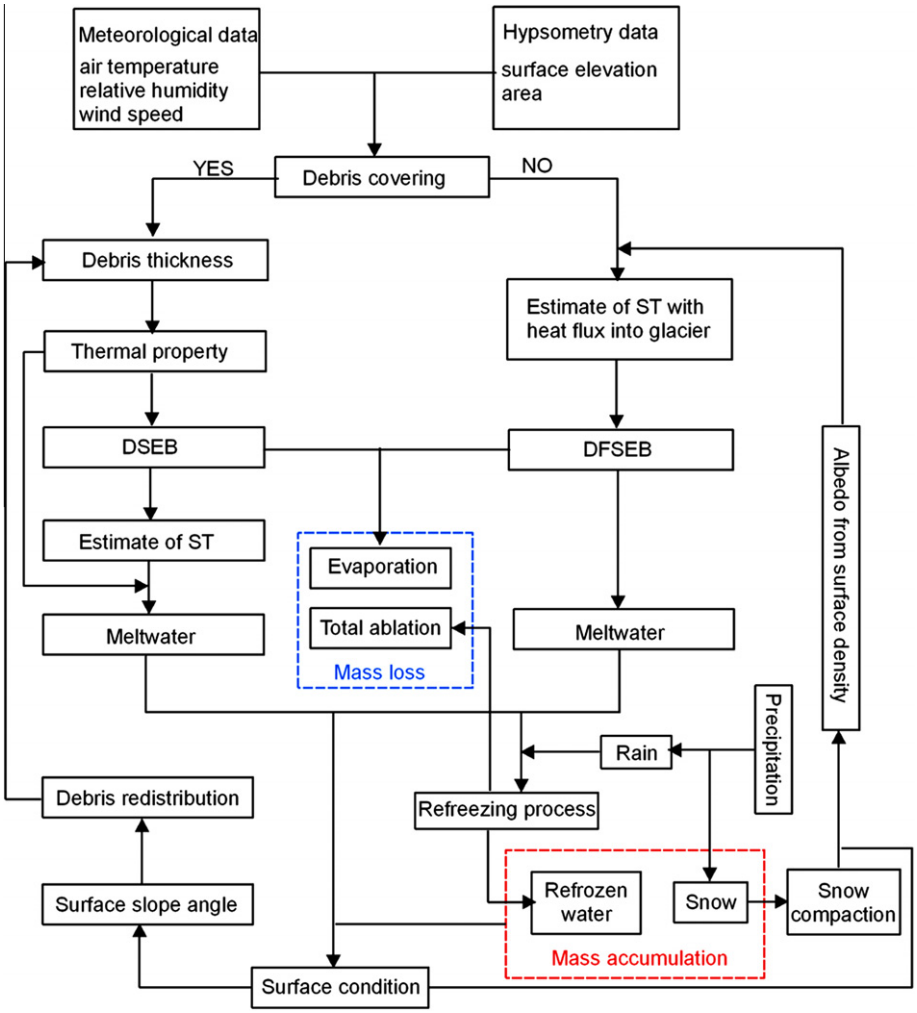

Fig. 2. Schematic structure of the surface energy–mass balance model. ST denotes the surface temperature. DSEB and DFSEB denote the surface energy balance of debris-covered and debris-free surfaces, respectively.

$$\log_{10}S^* = -15.32\times10^{-9}\rho^3 + 16.65\times10^{-6}\rho^2 - 7.30\times10^{-3}\rho + 3.23, \quad (10)$$

In Eq. (10), a meltwater effect is invoked when the snow temperature rises to 0 °C, and S^* will be decreased to 60% of its original value. The surface snow density ρ changes with snow densification, which is estimated using a model of snow densification established by Motoyama (1990). He suggested that the snow layer is densified due to viscous compression. The temporal variation in snow density is calculated from a compactive viscosity factor estimated by an empirical formula with respect to the density of a snow layer at a given depth and the overburden load exerted on that layer. The influence of water, which enhances snow compaction, is taken into account by changing the compactive viscosity factor for wet snow. The albedo of debris-free ice was set to 0.3 (Zhang et al., 2011), whereas that of the new snow was assumed to be 0.8 (Li and Su, 1996).

The downward short-wave radiation is calculated by using a method developed by Matsuda et al. (2006). They found a favorable correlation between precipitation and atmospheric transmissivity of solar radiation in terms of the monthly values on different glaciers of the Tibetan Plateau. This method was applied to the July 1st Glacier on the Tibetan Plateau where it performed well (Sakai et al., 2009). The relation between the monthly mean transmissivity and the monthly mean precipitation observed at the AWS during the period October 2008–July 2009 is shown in Fig. 3c. This is used to estimate the daily mean transmissivity, τ, from daily precipitation data. The downward short-wave radiation is then obtained from the daily mean transmissivity and the incoming short-wave radiation at the top of the atmosphere. As shown in Fig. 3d, short-wave radiation fluctuations are well simulated for the period May–September 2008, although the estimated short-wave radiation is greater than the observations that are <110 W m^{-2}. This is because the relation is established based on monthly data, for which low transmissivity data with high precipitation are not taken into account. In addition, glacier melt, which mainly determines the glacier mass balance, occurs when the short-wave radiation is large. Thus, overestimation of low short-wave radiation has little effect on the glacier mass balance estimate.

The surface temperature, T_S, is obtained to satisfy all heat balance equations by iterative calculation of the conductive heat flux, which is obtained by calculating the temperature profile of the snow layer and/or glacier ice. The melt rate of the debris-free ice, M, is calculated as

$$M = \frac{Q_M}{\rho_i L_f}, \quad (11)$$

where L_f is the latent heat of fusion (3.34×10^{-5} J kg^{-1}).

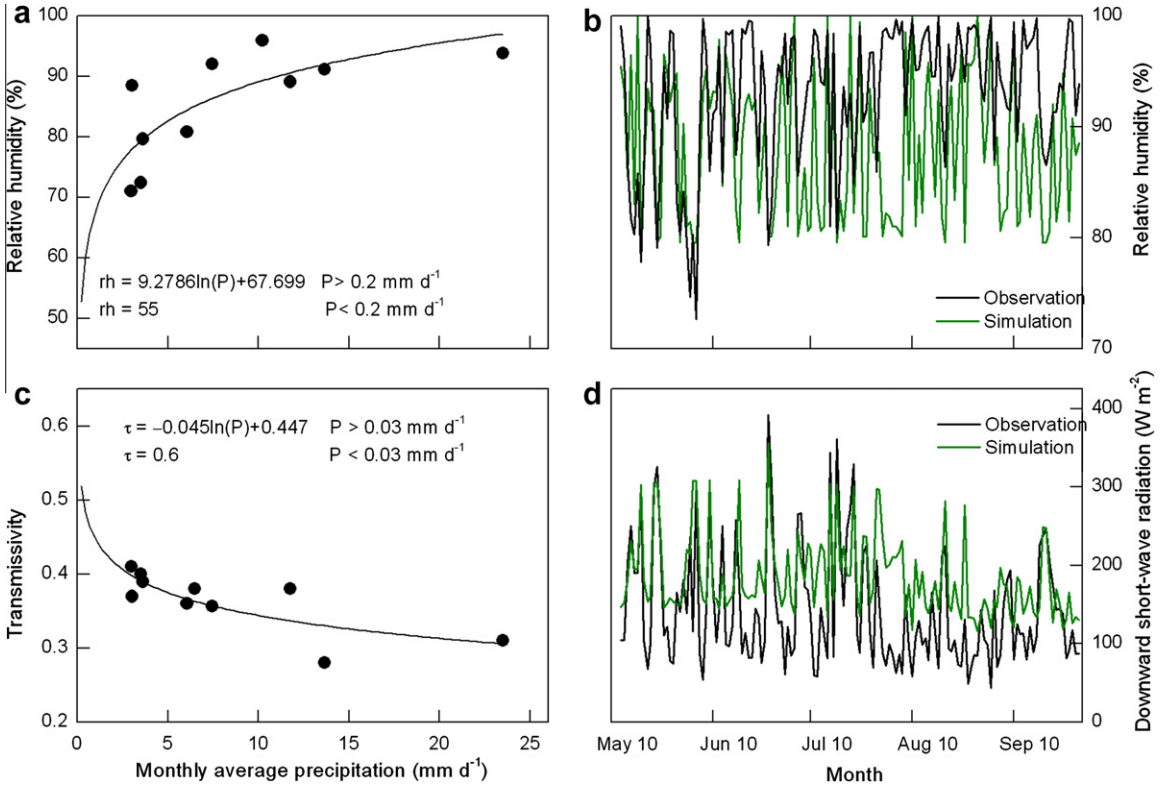

Fig. 3. (a) Relation between monthly precipitation and relative humidity observed from October 2008 to July 2009, (b) relative humidity observed from May to September 2008 and estimated using the relation shown in (a), (c) relation between monthly precipitation and monthly average transmissivity of solar radiation (downward short-wave radiation/short-wave radiation at top of the atmosphere), τ, observed from October 2008 to July 2009, and (d) daily solar radiation observed from May to September 2008 and its estimation using the relation shown in (c).

The catchment contains three debris-covered glaciers. The total debris-covered area accounts for 39% of the total ablation zone area of three glaciers. Fig. 1 shows the altitude-area distribution of debris-covered surfaces. At the debris-covered surface, the energy balance is expressed as

$$Q'_G = (1-\alpha')R_S + R_{Ld} + R_{Lu} + Q_S + Q_L + Q_R, \quad (12)$$

where Q'_G is the conductive heat flux into the debris layer, and the other energy components and calculations are the same as those mentioned above. All terms are taken to be positive toward the debris surface, in units of W m^{-2}. The albedo of the debris-covered surface, α', was set to 0.2 (Zhang et al., 2011). The only heat flux considered to reach the glacier ice is the conductive heat flux with simplifying assumption of a linear temperature profile within the debris layer and the constant heat flux stored in the debris layer from day to day. Therefore, the heat flux used for the ice melt, Q_M, can be calculated as

$$Q_M = Q'_G = \frac{(T'_S - T_I)}{R}, \quad (13)$$

where R is the thermal resistance of the debris layer (m^2 K W^{-1}), T'_S is the debris surface temperature (°C), and T_I is the ice temperature at the ice-debris surface, which was set to 0 °C (Zhang et al., 2011).

All energy-balance components at the debris-covered surface, except the short-wave radiation term, are explicitly determined from the debris surface temperature. The debris surface temperature, T'_S, can be calculated numerically by iteration. The resulting daily mean surface temperature is then used to calculate the rate of ice melt from Eqs. (11) and (13) for the prescribed thermal resistance of the debris layer. Zhang et al. (2011) found that the thermal resistance of the debris layer at a specific site could be regarded as constant usually in a melting season on Hailuogou Glacier. Therefore, the thermal resistance of the debris layer was assumed to be constant over the study period. Full details of the entire model have been reported by Zhang et al. (2011).

Some of the meltwater can be fixed to the glacier by refreezing if the glacier ice is cold enough (Fujita et al., 1996). Our calculations of the refreezing amount follow Fujita and Ageta (2000), which calculate the refreezing amount from considering the conduction of heat into the glacier ice and the snow layer and the presence of water at the interface between the snow layer and glacier ice. The refreezing amount R_F in the Fujita and Ageta (2000) scheme is given by

$$R_F = \frac{\rho_i c_i}{L_f}\int_{interface}^{z_c} \Delta T_Z dz + \frac{\rho_s c_i}{L_f}\int_{surface}^{interface} \Delta T_Z dz, \quad (14)$$

where ρ_s is the average density of snow (415 kg m^{-3}) (Aizen and Aizen, 1994; Liu et al., 1994), c_i = 2100 J kg^{-1} K^{-1} is the specific heat capacity of ice, z is the depth from the surface or snow-ice interface (m), z_c is the depth where the annual amplitude of ice temperature is <0.1 °C (assumed to be 20 m from the snow-ice interface), and ΔT_Z is the temperature difference of the snow/ice at a given depth during a given period (°C). In addition, refreezing during winter and shorter cooling events is considered by assuming the maximum water content as 5% in volume.

For each elevation band, snow accumulation is modeled from the precipitation value by using a simple temperature threshold to discriminate rain from snow. The threshold temperature was set to 2.0 °C (Liu et al., 2009). A mixture of snow and rain is assumed for a transition zone ranging from 1 K above and 1 K below the threshold temperature. Within this temperature range, the snow and rain percentages of total precipitation are obtained from linear interpolation. Redistribution of the original snowfall by wind transport or avalanches is not taken into account.

4.5. Model calibration

Model calibration involves constraining model parameters to get the best fit between the model simulations and the observed data. The parameters are adjusted within the accepted ranges according to one or more criteria that assess the goodness-of-fit between the simulated results and the observed data. In this study we use the observed runoff to optimize the precipitation gradient within the range from 12% to 60%. The calibration is performed to minimize the difference between observed and modeled runoff in different years. The precipitation gradient associated with the best agreement between observed and modeled runoff in different years is chosen. The presented model enables the estimation of the runoff from the catchment. The runoff contributions of all elevation bands are added to the total discharge at the outlet of the entire catchment. No routing between the spatial units and the river outlet is performed because the catchment has rather steep slopes (Fig. 1). This means that the runoff delay due to routing in the river network is thus much smaller than the given time step of one day. Liu et al. (2010) analyzed the water balance of the catchment using a hydrological method, and their results indicated that their method for calculating water balance of the catchment performed reasonably well without considering groundwater system and changes in evaporation and/or sublimation over the glacier surface, and the main contributions to the runoff were meltwater and rainfall. Furthermore, the runoff in the catchment shows a continuously increasing trend for the period 1994–2002, especially after 1997. The annual runoff reaches the maximum in 2002, which increases by 42% compared to the mean annual runoff over the period 1994–2002. Therefore, our model is calibrated against observed runoff in 1997 and 2002. The runoff, Q ($m^3\ s^{-1}$), can be calculated as

$$\begin{aligned} Q &= Q_1 + Q_2 \\ Q_1 &= M + P_{liq} - R_F\,, \\ Q_2 &= P_{tot} - E \end{aligned} \tag{15}$$

where Q_1 and Q_2 are the runoff from the glacier and glacier-free zone, respectively, P_{liq} is rain on the glacier, P_{tot} is the total precipitation, and E is the evaporation in the glacier-free zone calculated from the temperature and precipitation using the empirical equation of Kang et al. (1999). In addition, we assume there is no remaining snow at the end of the melt season, since our aim is to simulate the monthly runoff. Therefore, precipitation is not separated into rain and snow in the glacier-free zone.

Most mass balance models presented in previous studies are calibrated to get a good fit between observed and simulated variables by attempting to minimize a single measure of model performance (e.g. Oerlemans and Fortuin, 1992; Braithwaite and Zhang, 1999; Hock et al., 2007). However, there is no best criterion for statistically evaluating the quality of models because all models are simplifications of reality. Hence, calibration using a single criterion often constrains the model parameters to fit certain characteristics of the observed data, but neglects the remaining features. Here, we adopt multiple assessment criteria to assess the model performance. With the exception of the correlation coefficient r, three assessment criteria are used: the efficiency criterion R^2 (Nash and Sutcliffe, 1970), a modified version $R^2_{\ln}$ (Hock, 1999), and the root mean square error (RMSE). The criteria R^2 and RMSE have been widely used to measure the quality of fit between simulations and observations. The criterion $R^2_{\ln}$ is a measure of the agreement between simulations and observations emphasizing low-flow conditions. When the logarithms are found, discrepancies between modeled and observed runoff during peak flows exert less impact on the numerical value. The criteria, R^2 and $R^2_{\ln}$, assume a value of 1 in case of perfect agreement.

5. Results

5.1. Validation of global climate data

Unless otherwise stated, all significance levels of correlation coefficients (r) presented herein are $p < 0.001$. As shown in Table 2, daily, monthly, and annual H08 temperature and Y09 precipitation means correlate well with the corresponding observations from GAEORS, although correlation coefficients (r) for precipitation are lower than those for temperature. Daily, monthly, and annual H08 temperature means correlate well with the observations from GAEORS for the period 1988–2007, yielding coefficients of 0.90, 0.98, and 0.71, respectively, while analysis of the daily, monthly, and annual Y09 precipitation data yields correlation coefficients (r) of 0.70, 0.96, and 0.53, respectively. Seasonally, the correlations between the H08 and observed temperature are higher during the spring (March, April, May (MAM)), summer (June, July, August (JJA)), and autumn (September, October, November (SON)), compared to the winter (December, January, February (DJF)) (Table 2). Further analysis of the results reveals that the winter correlation is unduly influenced by the Decembers of 5 yrs (1998–2002) for which daily H08 temperatures are significantly larger than the observations, while the H08 and observed temperatures in December of other years show similar fluctuations, although there is a 433 m difference in elevation between the grid cell and GAEORS. If we remove the influence of the five exceptional Decembers, the correlation coefficient r during the winter rises to 0.85. This indicates that the H08 simulates winter temperatures reasonably well for the majority of years, and is able to capture the observed temporal variability well. Meanwhile, the Y09 precipitation data better capture the observed variability in spring (0.90), summer (0.70) and autumn (0.95) than in winter (0.53) (Table 2). Precipitation from spring to autumn accounts for 96% of the annual total in Hailuogou catchment, based on the observation during 1988–2004. The glaciers in the catchment are the summer-accumulation type glaciers (Shi and Liu, 2000). Thus, despite the lower correlation coefficient (r) during the winter, precipitation in winter may have little influence on the model performance.

Global climate data have to be corrected before use at the subgrid scale in the mass balance models. Hence the global climate data series used in this study are bias-corrected by Eqs. (2) and (3) which are established between in situ meteorological observations observed data and the global climate data over the period 1988–1997. Fig. 4a and b shows the bias-corrected and observed daily temperature averaged over the period 1998–2007 and precipitation averaged over the period 1998–2004. The correlation coefficient (r) between the bias-corrected and observed daily temperature is 0.96 with the RMSE value of 1.54 °C, and the correlation coefficient (r) between the bias-corrected and observed daily precipitation is 0.87 with the RMSE value of 0.001 m. Fig. 4c and d show the variations in the bias-corrected and observed monthly temperature over the period 1998–2007 and annual precipitation over the period 1988–2004. As can be seen, bias-corrected global climate data yields good agreement with the observations.

Overall, the above analysis suggests that the global gridded temperature and precipitation data used in this study correspond sufficiently well with the observations at GAEORS to be used as input for mass balance model in Hailuogou catchment.

5.2. Model calibration and verification

Fig. 5 shows the best solution found for the runoff simulation in different years, and the fit between observed and modeled runoff, as measured by the efficiency criterion R^2, its modified version $R^2_{\ln}$ and the RMSE. The results of model calibration show that there is

Table 2
Correlation coefficients (r) between the global climate data and observations from GAEORS. All significance levels of correlation coefficients presented herein are $p < 0.001$.

	Temperature[a]	Precipitation[b]
Daily	0.90	0.70
Monthly	0.98	0.96
Annual	0.71	0.53
Spring (May, April, May (MAM))	0.98	0.90
Summer (June, July, August (JJA))	0.91	0.70
Autumn (September, October, November (SON))	0.99	0.95
Winter (December, January, February (DJF))	0.64	0.53

[a] Data were used for the period 1988–2007.
[b] Data were used for the period 1988–2004.

close agreement between observed and modeled monthly runoff, yielding $R^2 > 0.9$, $R^2_{ln} > 0.7$ for using observed meteorological data, and $R^2 > 0.9$, $R^2_{ln} > 0.9$ for using global climate data (Fig. 5). The runoff simulations in 1997 and 2002 by using observed meteorological data and global climate data have small RMSE values compared to the corresponding mean monthly discharge of 8.1 $m^3 s^{-1}$ and 13.7 $m^3 s^{-1}$ (Fig. 5). This indicates that the precipitation gradient of 18% per 100 m can give a good agreement between observed and modeled runoff, and is therefore selected as the best solution for further analysis.

The calibrated model (Fig. 5) is verified against an independent set of runoff data collected over the periods 1994–1996 and 1998–2001. Scatter diagram of observed and modeled monthly runoff is shown in Fig. 6, along with a plot of the corresponding cumulative variation. Overall, the calibrated model performs well in the validation period. The efficiency criterion R^2 and its modified version R^2_{ln} are respectively 0.84 and 0.80 for observed meteorological data, and 0.84 and 0.86 for global climate data (Fig. 6a). The monthly runoff simulations using observed meteorological data and global climate data have small RMSE values compared to the mean monthly discharge of 13.4 $m^3 s^{-1}$, which equal to 2.68 and 2.7 $m^3 s^{-1}$, respectively. As shown in Fig. 6b, the model performs well with respect to the cumulative runoff over the period 1994–2002. The cumulative runoff simulated using observed meteorological data is underestimated by 10% over the period 1994–2002, whereas that simulated using global climate data is overestimated by 4% at the same period. As a result, the modeled cumulative runoff can capture the long-term trend.

The calibrated model allows for the effect of debris cover on glacier ablation, which is verified by comparing the model results to observations measured at stakes on Hailuogou Glacier in different periods. Scatter diagrams of modeled and measured ablation at

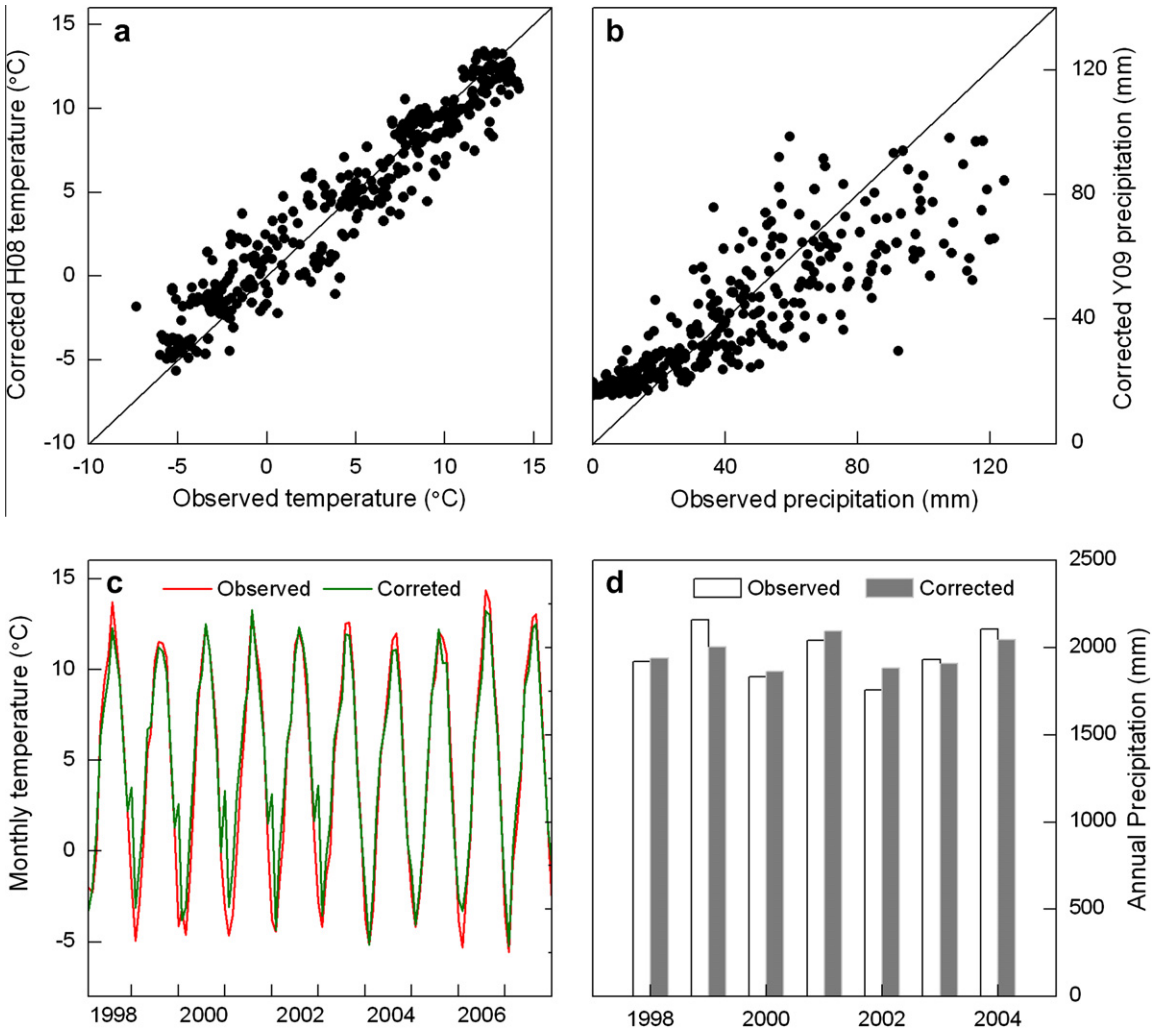

Fig. 4. (a) Observed daily air temperature and bias corrected H08 temperature averaged over the period 1998–2007, (b) observed daily precipitation and bias-corrected Y09 precipitation averaged over the period 1998–2004, (c) comparison of observed monthly temperature and bias-corrected H08 temperature over the period 1998–2007, and (d) comparison of observed and corrected annual precipitation over the period 1998–2004.

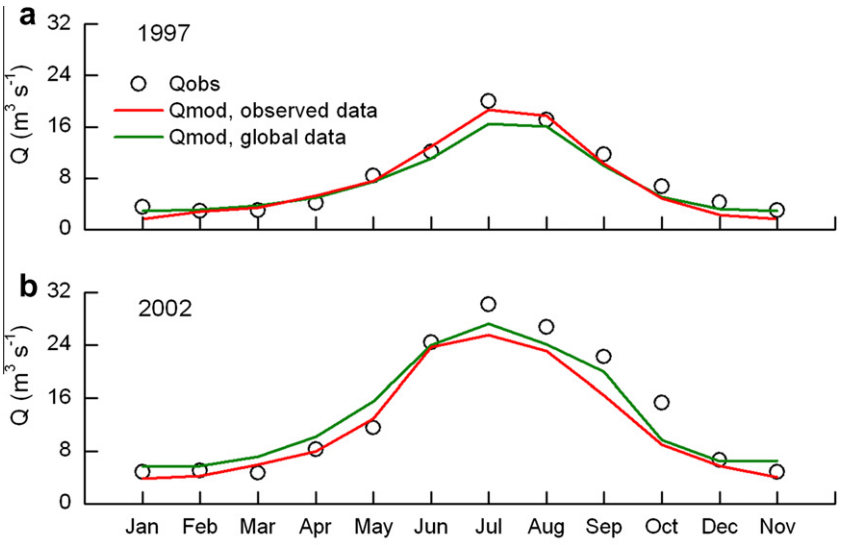

	1997		2002	
	Observed data	Global data	Observed data	Global data
R^2	0.95	0.94	0.94	0.96
R_{ln}^2	0.73	0.93	0.94	0.91
RMSE	1.10	0.79	2.20	2.10

Fig. 5. Observed and modeled runoff of the catchment in 1997 (a) and 2002 (b) using the optimized precipitation gradient with respect to the assessment criteria (R^2, R_{ln}^2 and RMSE ($m^3 s^{-1}$)). Qmod, observed data and Qmod, global data denote the simulations using the meteorological observations and global climate data, respectively.

stakes in different periods are shown in Fig. 7. Overall, the model performs well at stake locations with the RMSE value of 0.003 m w.e. d^{-1}, compared to the mean melt rate of 0.03 m w.e. d^{-1}. The overall correlation coefficient r between measured and modeled ablation in different periods is 0.78 (Fig. 7a). In particular, the correlation coefficient r between measured and modeled ablation in the summer of 2008 is 0.82 (Fig. 7b). However, the calibrated model overestimates the low melt rates beneath the thick debris layer (Fig. 7a). This may be influenced by the water content of the thick debris layer. The water content of the debris layer exerts a strong influence on the melt rate beneath the debris layer through affecting its thermal properties (Nakawo and Young, 1981). Nakawo and Young (1981) found that the thermal conductivity of the debris layer increases with the water content of the layer increasing, resulting in the melt rate beneath the debris layer increasing. They also found that modeled melt rates for dry thick debris is larger than those for saturated thick debris. However, considering the effect of the water content must allow the physical properties of the debris layer to vary with depth, which would require detailed data on internal debris temperature and water content, and these properties are difficult to determine for an entire glacier. Hence, this property is unlikely to be known in any practical application of the model presented in previous studies (e.g. Nakawo and Young, 1981; Nicholson and Benn, 2006; Reid and Brock, 2010). In this study we calculate the melt rate to most closely approximate the measurements without considering the nature of the water content of the debris layer, despite the fact that the debris may be saturated where the layer is thick, and moist where it is thicker, so the measurements will be expected to plot closer to the modeled results for saturated debris. This pattern suggests that the model systematically overestimates the melt rate in this environment. Despite this uncertainty, overall, the model can produce reliable estimates of ablation beneath the debris layer on an annual timescale (Fig. 7) and allows us to consider the effect of debris cover on modifying the catchment mass balance.

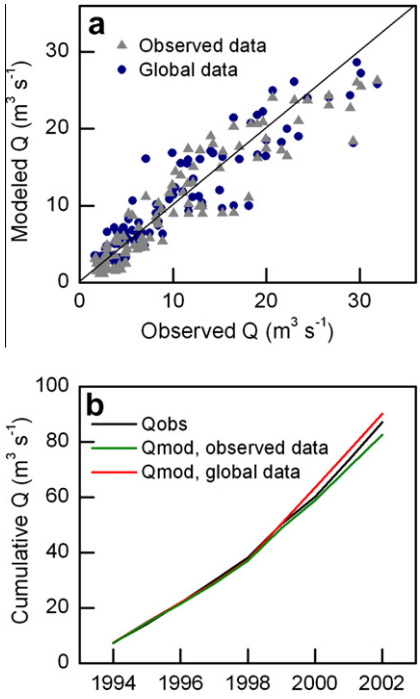

Fig. 6. Evaluation of the calibrated model using scatter diagrams of observed versus modeled monthly runoff (a) and cumulative runoff (b). Qmod, observed data and Qmod, global data denote the simulations using the meteorological observations and global climate data, respectively.

Overall the calibrated model performs well and can simulate the observations accurately. This indicates that the model has predictive power for mass balance modeling on a catchment scale, assuming that the calibrated model parameter is valid for different

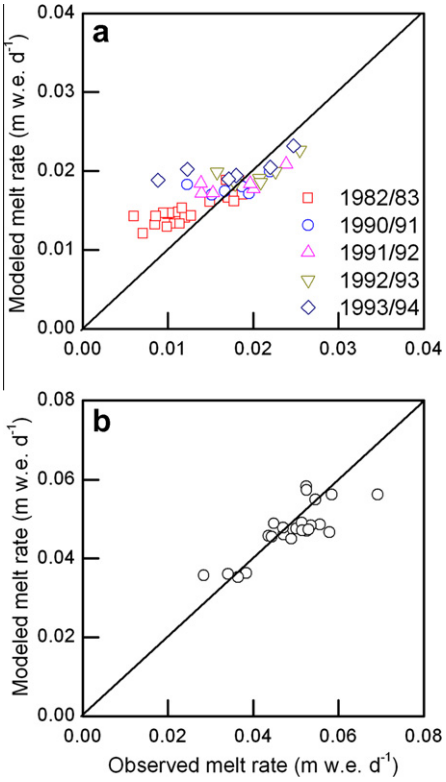

Fig. 7. Evaluation of the calibrated model using scatter diagrams of observed vs modeled stake ablation on Hailuogou Glacier in 1982/83, 1990–1994 (a), and the summer of 2008 (b).

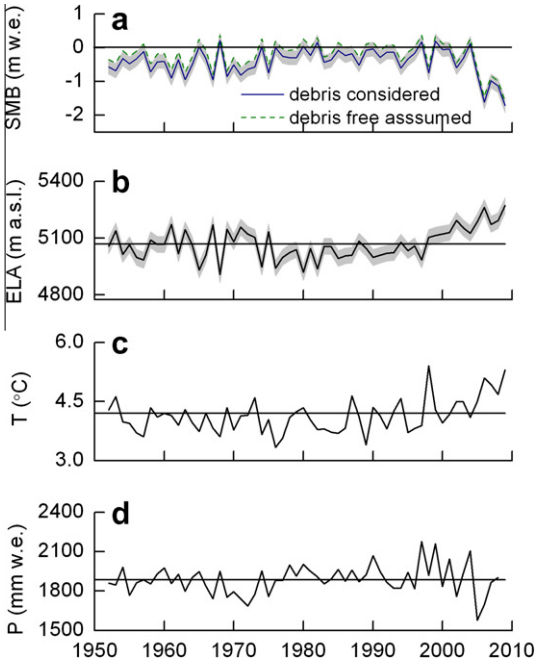

Fig. 8. (a) Calculated specific mass balance (SMB) showing both the debris-covered surface and the assumed debris free on glaciers, (b) calculated equilibrium line altitude (ELA), (c) mean annual temperature (T), and (d) annual precipitation (P). Light gray shading for the SMB and ELA denotes the standard deviation. Lines in (b), (c), and (d) denote the average values of ELA, T and P over the period 1952–2009.

time periods. In particular, the model is able to reliably estimate glacier ablation beneath debris, allowing us to consider the influence of debris on the mass balance of the catchment. We evaluate the use of global climate data for modeling in Hailuogou catchment and found that accurate estimation of catchment mass balance is possible using these data (Fig. 4).

5.3. Mass balance reconstruction

We calculate the long-term mass balance and ELA for Hailuogou catchment using observed climate data (1989–2009) extended with global climate data (H08 and Y09) (1951–1988) (Fig. 8). The ELA is calculated as the altitude where the annual mass balance is zero. The annual mass balances of Hailuogou catchment are consistently negative (Fig. 8a), with eight positive balance years over the 58 yrs period (1952–2009), varying between 0.19 and −1.72 m w.e. The mean annual mass balance in the whole catchment is −0.42 m w.e. for the period 1952–2009. In particular, in recent years (2001–2009) the mean mass balance is −0.79 m w.e., about 2.3 times the mean value during 1952–2000 (−0.35 m w.e.). The cumulative mass balance of the catchment is −24.3 m w.e. for the period 1952–2009. In recent years (2001–2009), the cumulative mass balance of the catchment accounts for 30% of the total cumulative mass balance for the period 1952–2009. The ELA trend of Hailuogou catchment over the period 1952–2009 is shown in Fig. 8b. The ELA of the glaciers in the catchment varies between 4907 and 5273 m a.s.l. during the study period, with a mean of 5068 m a.s.l. The ELA of the glaciers shows a slight negative trend with a rate of −0.5 m yr^{-1}during 1952–2000. In contrast, glaciers show a significant positive trend (12.3 m yr^{-1}) of the ELA during 2001–2009 (Fig. 8b). This indicates that the ascending ELA results in an acceleration of glacier wastage in Hailuogou catchment in recent years.

6. Discussion

6.1. Model uncertainty

In highly glacierized catchments, major challenges for mass balance simulation are the lack of available precipitation data and the large spatial variability of precipitation due to orographic effects. Furthermore, the precipitation gradient is difficult to estimate, which makes spatial interpolation challenging. In this study, the precipitation increase with altitude is set to a fixed gradient that is optimized by the calibration procedure, minimizing errors between the model results and observations. However, uncertainties still arise due to the high spatial variability of precipitation, and the precipitation gradient is optimized to the mean conditions over the entire study period. In particular, when applying such gradient to all years, larger model errors are to be expected for years when the observations have larger deviations from the mean conditions. However, the model predictive ability for long-term mass balance would be substantially reduced without a generalized parameter set for the entire study period. The main aim of this study is to develop a simple approach that considers the significance of debris cover and its influence for accurate estimation of the long-term variation and trend in surface mass balance on the catchment scale. Hence, a generalized parameter set was not unexpected to be used for the mass balance calculation in Hailuogou catchment.

Glacier area data are generally not available every year. Some studies assumed the constant glacier area in their mass balance calculations (e.g. Fischer, 2009; Fujita et al., 2011). Hirabayashi et al. (2010) presented an approach in which the glacier area per elevation band is updated daily. In our analysis, glacier areas in 1966, 1975, 1994, and 2007 are used. These are correspondingly assumed to be constant over the periods 1952–1966, 1967–1975, 1976–1994, and 1995–2009. As reported by Liu et al. (2010), the glacier area of the catchment decreased by 2.9 km^2 during 1966–2007 (7.8% of the 1966 total area), which mainly occurred in the lower part of the glaciers. To assess the uncertainties in constant

glacier areas in different periods, the mass balance during the entire analysis period is calculated using the glacier areas in 1966, 1975, 1994, and 2007, respectively. The resulting mass balance indicates that the specific mass balances estimated using the glacier areas of 1966, 1975, and 1994 are more negative by 0.06, 0.07, and 0.04 m w.e. (the average of the calculation period), respectively, compared to those estimated by using the glacier areas in 1975,1994, and 2007. This finding indicates that changes in glacier extent during the periods 1952–1966, 1967–1975, 1976–1994, and 1995–2009 have a small impact on the specific mass balance of Hailuogou catchment.

6.2. Effect of supraglacial debris on glacier mass balance and runoff

Hailuogou catchment is dominated by debris-covered glaciers (Table 1). The total debris-covered area accounts for 39% of the total area of ablation zones of three debris-covered glaciers in the catchment. Zhang et al. (2011) extensively surveyed the debris thickness on Hailuogou Glacier, where the debris-covered area accounted for 41% of the total area of the ablation zone. They suggested that the debris thickness varies from just several millimetres of patchy cover to >1 m, with an inhomogeneous spatial distribution. As suggested by previous studies, dispersed and thin debris enhances ice melt rates through albedo reduction, whereas debris cover of thickness exceeding a few centimetres reduces ice melt by insulating the ice from atmospheric heat (Østrem, 1959; Nakawo and Young, 1981; Mattson et al., 1993). Zhang et al. (2011) found that because of the inhomogeneous distribution of debris thickness, about 67% of the ablation area on Hailuogou Glacier has undergone accelerated melting, whereas about 19% of the ablation area has experienced inhibited melting, and the sub-debris melt rate equals the bare-ice melt in only 14% of the ablation area; on the other hand, the altitude distribution of the debris thickness further complicated the ablation gradient on the ablation area, making it completely different to that of debris-free glaciers. Therefore, spatial distribution of debris plays a crucial role in the estimation of glacier ablation, and must be considered in the mass balance estimation of Hailuogou catchment. To assess the effect of the debris cover on the mass balance of Hailuogou catchment during the past few decades, we recalculate the mass balance assuming that there is no debris on the three glaciers in the catchment. In accordance with the calculation, we find a 12% increase of glacier melt under the real surface condition during 1952–2009 compared to that with an assumption of no debris cover on the glaciers. As a result, the positive mass balance years account for 35% of all years (58 yrs) without debris cover on the glaciers, but they represent only 14% of all years under the real surface conditions (Fig. 8a). The change in mean mass balance with the real surface condition during 1952–2009 is twice as much as that without debris cover on the glaciers (−0.21 m w.e.). This indicates that supraglacial debris cover significantly accelerates mass loss from the glaciers in Hailuogou catchment (Fig. 8a).

Scherler et al. (2011; Fig. 2) reported that widespread debris cover on many Himalayan glaciers reduces their retreat rates, making their fronts stable, which are therefore unsuitable as indicators of recent climate change. In contrast, the termini of the debris-covered glaciers in Hailuogou catchment have been retreating at a high rate during the past few decades (Su et al., 1992; Liu et al., 2010; Zhang et al., 2010). The terminus of Hailuogou Glacier receded at a mean annual rate of 27.4 m yr^{-1} during 1998–2008 (Zhang et al., 2010), and Glacier No. 2 receded at a mean annual rate of 30.0 m a^{-1} during the period 1981–1990 (Su et al., 1992). Based on the glacier outlines in 1966 and 2007 created by Liu et al. (2010), we calculate the retreat rates of the termini of seven glaciers in the catchment. The mean annual retreat rate of the termini of three debris-covered glaciers is ~28.9 m yr^{-1} during 1966–2007, which is significantly larger than that of four debris-free glaciers (~15.6 m yr^{-1}). The analysis of the spatial characteristics of the ice melt rates on the ablation area of Hailuogou Glacier indicated that one of the high melt rates occurs in the terminus zone (altitudes of 3000–3200 m a.s.l.), an area with a wide distribution of coexisting debris-covered ice, bare ice, ice cliffs, and supraglacial ponds (Zhang et al., 2011). Such coexisting surface that is composed of debris-covered ice, bare ice, ice cliffs and supraglacial ponds, is also widely distributed in the terminus zones of other debris-covered glaciers in the catchment (Li and Su, 1996). In these areas, in addition to debris cover and its spatial distribution impacting the ice melt rate, ice cliffs and supraglacial ponds significantly accelerate the ice melt rate (Sakai et al., 2000, 2002). Ice cliffs are generally covered with a thin layer of debris or dust, meaning that the melt rate is higher than on nearby debris-covered surface (Sakai et al., 2000, 2002). The analysis of a pond heat budget indicates that the energy absorption at the supraglacial pond is several times larger than that at the surrounding debris-covered surface, which results in accelerating the ice melt rate (Sakai et al., 2000). Hence, spatial distribution of the areas with the coexisting debris-covered ice, bare ice, ice cliffs, and supraglacial ponds leads to the spatially inhomogeneous ice ablation, which is likely to make a disproportionately large contribution to ablation at the glacier termini. On the other hand, supraglacial ponds can accelerate glacier terminus disintegration by exposing ice faces at the surface (Röhl, 2008) and lowering of the glacier surface (Sakai and Fujita, 2010). Due to the inhomogeneous ablation, the debris layer becomes increasingly unstable in these areas (Iwata et al., 2000; Benn et al., 2001), releasing debris via occasional sluicing of debris down steep slopes. This process redistributes the debris upon the glacier surface, and then modifies the spatial variability in the ice melt rate, causing differential surface lowering, development of ice cliffs and evolution of supraglacial ponds (Iwata et al., 2000; Benn et al., 2001; Sakai et al., 2000, 2002; Röhl, 2008; Sakai and Fujita, 2010). Furthermore, the ice velocity is relatively large on debris-covered glaciers in the catchment (Li and Su, 1996; Zhang et al., 2010). Ice velocities measured on Hailuogou Glacier indicated that the ice velocity at the terminus is ~28.8 m yr^{-1} (Zhang et al., 2010), which is significantly larger than that in the Himalayan study of Scherler et al. (2011). Consequently, debris and its spatial distribution in association with ice cliffs and supraglacial ponds results in the unstable fronts of debris-covered glaciers in this catchment, which accelerates their terminus disintegration and retreat.

The main contributions to the runoff of Hailuogou catchment are meltwater and rainfall (Liu et al., 2010). Note that glacier meltwater is the main contribution to the increasing runoff of the catchment during 1994–2002 when the precipitation of the catchment shows a decrease trend (Fig. 8d). As discussed above, Hailuogou catchment is dominated by debris-covered glaciers, where the ice melting depends strongly on debris thickness and its spatial continuity. To assess the effect of the debris cover on the runoff in the catchment, we recalculate the runoff assuming that there is no debris on three debris-covered glaciers. In accordance with the calculation, we find that the mean annual runoff without debris cover on three glaciers during 1994–2004 decreases by 6% compared to that with the real surface condition. In addition, evaporation of rainwater from debris appears to have a small influence on catchment hydrology and downstream water resources (Brock et al., 2010). It is apparent that the presence of debris cover leads to an increase in catchment runoff through its influence of accelerating surface melt, and its insulation effect is not significant in Hailuogou catchment.

6.3. Climate change, mass balance, and ELA

During the past 58 yrs (1952–2009), glaciers in Hailuogou catchment experience significant mass loss (Fig. 8a), especially in

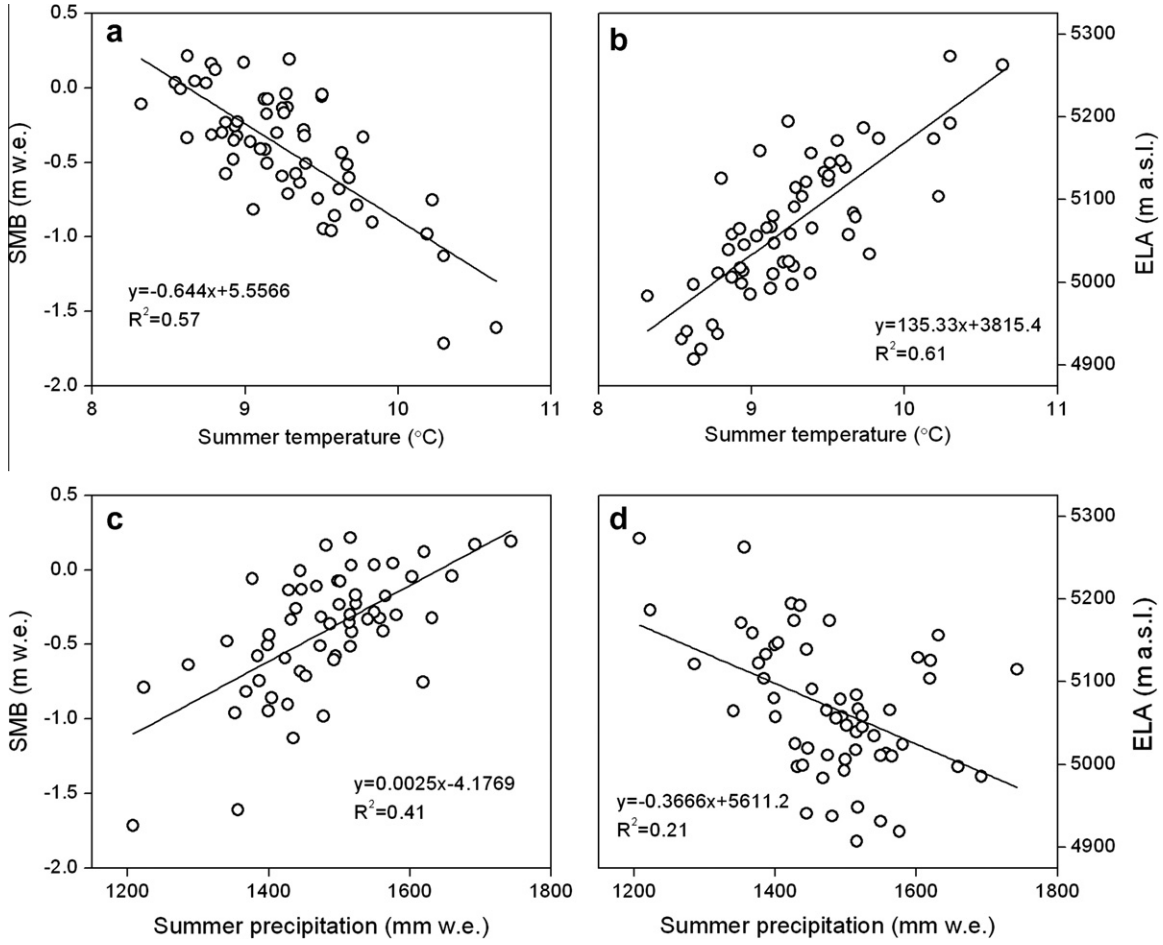

Fig. 9. (a and b) Regression relations of summer temperature vs the specific mass balance (SMB) and the ELA, and (c and d) regression relations of summer precipitation versus the SMB and the ELA for the period 1952–2009. Here, R^2 is the coefficient of determination.

Table 3
Mass balance (MB; m w.e.), summer temperature (Temp.; °C), and precipitation (Prec.; mm), and their contributions to the glacier mass balance in each decade estimated based on the regressions shown in Fig. 9.

	Temp.	Prec.	MB	Variable contribution (%)	
				Temp.	Prec.
1950s	9.09	1473.1	−0.41	19.6	80.4
1960s	9.19	1450.9	−0.51	35.9	64.1
1970s	9.02	1449.7	−0.36	−15.2	115.2
1980s	9.05	1513.9	−0.20	–	–
1990s	9.46	1541.2	−0.21	135	−35
2000s	9.82	1508.9	−0.78	97.5	2.5

the last 10 yrs. These findings agree with those of Liu et al. (2010) and Zhang et al. (2010), who reported an accelerated shrinkage of glaciers in the last few decades based on topographic maps, remote sensing data, and the GAEORS meteorological data. The glaciers in this catchment are the summer-accumulation type, which is more sensitive to climate change (Shi and Liu, 2000). As shown in Fig. 8c, the air temperature of the catchment shows a significant increasing trend with a rate of 0.13 °C $(10\,yr)^{-1}$ over the period 1952–2009, especially in the last 20 years when the rate was 0.27 °C $(10\,yr)^{-1}$. In addition, the air temperature at the beginning of the melt season (April) and at its end (October) rose by 1.6 and 0.9 °C, respectively, for the period 1998–2004 compared to those for the period 1988–1997 (Zhang et al., 2010). This possibly prolongs the melt period and causes a significant decrease in snow accumulation, and an additional decrease in surface albedo due to a diminished summer snowfall that prevents the absorption of solar radiation and snow melt during the melt season (Fujita, 2008). On the other hand, the annual precipitation shows a slight increasing trend during 1952–2009 (Fig. 8d). As shown in Fig. 8d, annual precipitation is relatively low in the 1950s, 1960s, and 1970s, but high in the 1980s and 1990s. After 2000 annual precipitation decreases compared to that in the 1990s. In addition, the precipitation from July to September decreased by 24% for the period 1998–2004 compared to that for the period 1988–97, especially in July and September (Zhang et al., 2000). This change possibly has a significant effect on glacier accumulation in the catchment.

To quantify the effect of climate change on glaciers in the catchment, we examine the relationships among summer (May–October) temperature, precipitation, mass balance and ELA. Figs. 9a and b shows the relations between summer temperature and the mass balance and ELA, respectively. Summer temperature is negatively correlated with the mass balance and positively associated with the ELA. The regression results in Fig. 9a and b suggest that the 1 °C summer temperature change results in 0.644 m w.e. glacier mass loss, and 135.3 m ELA ascending, respectively. Similarly, summer precipitation is positively correlated with the mass balance and negatively associated with the ELA (Fig. 9c and d). The regression results in Fig. 9c and d suggest that the 100 mm summer precipitation change leads to 0.25 m w.e. mass accumulation, and 36.7 m ELA descending, respectively. Compared to the precipitation-mass balance/ELA relations, those between air

temperature and mass balance/ELA are stronger, especially in recent years. Therefore, we can investigate which variables have controlled the glacier mass balance in each decade using the 1980s as a reference decade. As shown in Table 3, summer precipitation is significantly reduced in the 1950s, 1960s, and 1970s compared to in the 1980s, and summer temperature shows a slight variation over the same period. Based on the regression results mentioned above, a marked reduction in summer precipitation that was observed before the 1980s appears to be the main cause of the negative mass balance. After the 1980s, the summer temperature shows a significant increasing trend, and the precipitation shows a slight increasing trend in the 1990s and a slight decreasing trend in the 2000s (Table 3). Increasing summer temperature is the main cause of rapid wasting of the glacier mass in Hailuogou catchment (Table 3). In particular, the contribution of the rise in temperature to glacier mass loss increases to 97.5% in the 2000s (Table 3). This indicates that temperature change controls variation in glacier mass balance in Hailuogou catchment over the last 20 yrs.

7. Conclusions

A surface energy–mass balance model is implemented on a catchment scale, and the significance of debris and its influence on glacier melt rates is taken into account. The model is used to reconstruct the mass balance time series of glaciers in Hailuogou catchment in the south-eastern Tibetan Plateau, where there are three debris-covered and four debris-free monsoonal maritime glaciers. Global climate data (1952–1988) and observations (1989–2009) are used to drive the model. The global climate data are validated against long-term meteorological observations from Hailuogou catchment and correspond sufficiently well with surface observations to be used for mass balance modeling. The model is calibrated against runoff observations in the catchment using multiple assessment criteria to minimize the error between simulations and observations. It is verified by comparing the model results to the observed runoff and the ablation measured at stakes in different periods. Overall, the calibrated model performs well, which indicates that the model has predictive power for mass balance modeling on a catchment scale, assuming that the calibrated model parameter is valid for different time periods. In particular, the model is able to reliably estimate glacier ablation beneath debris, allowing us to consider the effect of debris on the mass balance of the catchment.

From the reconstructed time series, a mass loss of −24.3 m w.e. is estimated in Hailuogou catchment over the period 1952–2009. The annual mass balances are consistently negative over the 58-yr period with eight positive balance years. In particular, glaciers in the catchment show markedly rapid wastage with an associated increasing trend of the ELA in recent years (2001–2009). Regression analyses show that the relations between summer temperature and mass balance/ELA are much stronger relative to the precipitation-mass balance/ELA relations. On the basis of these regression relations, we found that a marked reduction in summer precipitation is the main cause of the negative mass balance before the 1980s, whereas significant warming in the summer is the main cause of rapid wasting of the glacier mass in the catchment in recent decades. In addition, recalculation with an assumption of no debris cover on the glaciers in the catchment indicates that the presence of debris results in the 12% increase of glacier melt during 1952–2009, and then significantly accelerates glacier mass loss. Furthermore, debris and its spatial distribution in association with ice cliffs and supraglacial ponds results in the unstable fronts of debris-covered glaciers in Hailuogou catchment.

Debris-covered glaciers are not restricted to the Tibetan Plateau, but are common in many other mountain ranges around the world. For modeling mass balance, predicting runoff and response to climate change, debris cover and its influence on glacier melt rates should be added to analysis that has determined glacier mass balances. Using the energy–mass balance model presented in this study, we can accurately estimate the long-term variation and trend in surface mass balance on a catchment scale and examine the significance of debris cover and its influence on glacier melts. The model can also output catchment runoff. The global climate data used in this study can be used to drive such a model. This means that the model can be applied to other catchments in the Tibetan Plateau, where debris-covered glaciers exist, to investigate glacier response to climate change and the impact of global warming on the regional water cycle, even in regions that are not routinely monitored because of the harsh climatic conditions and remoteness.

Acknowledgements

We thank to Trend Biggs, Koji Fujita and the anonymous reviewer for their extensive and very helpful comments and suggestions. We also thank the Gongga Alpine Ecosystem Observation and Research Station of the Chinese Ecological Research Network for providing the meteorological data. This research was supported by the Global Change Research Program of China (2010CB951401), the National Natural Science Foundation of China (40701032, 40801030), and the Funding Program for next generation world-leading researchers, JSPS and CREST project of Japan Science and Technology Agency (JST).

References

Aizen, V.B., Aizen, E.M., 1994. Regime and mass-energy exchange of subtropical latitude glaciers under monsoon climatic conditions: Gongga Shan, Sichuan. China. J. Mt. Res. Dev. 14 (2), 101–118.

Arnold, N.S., Willis, C., Sharp, M.J., Richards, K.S., Lawson, W.J., 1996. A distributed surface energy balance model for a small valley glacier: I. Development and testing for Haut Glacier d'Arolla, Valais, Switzerland. J. Glaciol. 42 (140), 77–89.

Barry, R.G., 2006. The status of research on glaciers and global glacier recession: a review. Prog. Phys. Geogr. 30, 285–306. http://dx.doi.org/10.1191/0309133306pp 0309133478ra.

Benn, D.I., Wiseman, S., Hands, K.A., 2001. Growth and drainage of supraglacial lakes on the debris-mantled Ngozumpa Glacier, Khumbu Himal. Nepal. J. Glaciol. 47 (159), 626–638.

Bougamont, M., Bamber, J.L., Greuell, W., 2005. A surface mass balance model for the Greenland ice sheet. J. Geophys. Res. 110, F04018. http://dx.doi.org/10.1029/2005JF000348.

Braithwaite, R.J., Zhang, Y., 1999. Modelling changes in glacier mass balance that may occur as a result of climate changes. Geogr. Ann. 81A, 489–496.

Braun, L.N., Grabs, W., Rana, B., 1993. Application of conceptual precipitation runoff model in the Langtang Khola Basin, Nepal Himalaya. In: Young, G.J. (Eds.), Snow and Glacier Hydrology. IAHS Publication, Proceedings of the Kathmandu Symposium, November 1992, pp. 221–237.

Brock, B.W., Mihalcea, C., Kirkbride, M.P., Diolaiuti, G., Cutler, M.E.J., Smiraglia, C., 2010. Meteorology and surface energy fluxes in the 2005–2007 ablation seasons at the Miage debris-covered glacier, Mont Blanc Massif, Italian Alps. J. Geophys. Res. 115, D09106. http://dx.doi.org/10.1029/2009JD013224.

Cao, Z., Cheng, G., 1994. Preliminary analyses of hydrological characteristics of Hailuogou Glacier on the eastern slope of the Gongga Mountain. In: Xie, Z., Kotlyakov, V.M. (Eds.), Glaciers and Environment in the Qinhai-xizang (Tibet) Plateau (I) – The Gongga Mountain. Science Press, Beijing and New York, pp. 143–156.

Cheng, G., 1996. Exploration of precipitation features on extra-high zone of Mt Gongga. Mt. Res. 14 (3), 177–182 (In Chinese with English abstract).

Dyurgerov, M.B., Meier, M.F., 2005. Glaciers and the changing earth system: a 2004 snapshot. Occasional Paper 58, Institute of Arctic and Alpine Research, University of Colorado at Boulder, Boulder, Colorado, USA.

Fan, Y., van den Dool, H.V.D., 2008. A global monthly land surface air temperature analysis for 1948-present. J. Geophys. Res. 113, D01103. http://dx.doi.org/10.1029/2007JD008470.

Fischer, A., 2009. Glaciers and climate change: interpretation of 50 years of direct mass balance of Hintereisferner. Global Planet. Change 71, 13–26. http://dx.doi.org/10.1016/j.gloplacha.2009.11.014.

Fujita, K., 2007. Effect of dust event timing on glacier runoff: sensitivity analysis for a Tibetan glacier. Hydrol. Process. 21 (21), 2892–2896. http://dx.doi.org/10.1002/hyp. 6504.

Fujita, K., 2008. Effect of precipitation seasonality on climatic sensitivity of glacier mass balance. Earth Planet. Sci. Lett. 276, 14–19. http://dx.doi.org/10.1016/j.epsl.2008.08.028.

Fujita, K., Ageta, Y., 2000. Effect of summer accumulation on glacier mass balance on the Tibetan Plateau revealed by mass–balance model. J. Glaciol. 46 (153), 244–252.

Fujita, K., Nuimura, T., 2011. Spatially heterogeneous wastage of Himalayan glaciers. PNAS 108 (34), 14011–14014. http://dx.doi.org/10.1073/pnas.1106242108.

Fujita, K., Seko, K., Ageta, Y., Pu, J., Yao, T., 1996. Superimposed ice in glacier mass balance on the Tibetan Plateau. J. Glaciol. 42 (142), 454–460.

Fujita, K., Takeuchi, N., Nikitin, S.A., Surazakov, A.B., Okamoto, S., Aizen, V.B., Kubota, J., 2011. Favorable climatic regime for maintaining the present-day geometry of the Gregoriev Glacier, Inner Tien Shan. TC 5, 539–549. http://dx.doi.org/10.5194/tc-5-539-2011.

Fukushima, Y., Kawashima, K., Suzuki, M., Ohta, T., Motoyama, H., Kubota, H., Yamada, T., Bajracharya, O.R., 1987. Runoff characteristics in three glacier-covered watersheds of Langtang Valley, Nepal Himalaya. Bull. Glaciol. Res. 5, 11–18.

Hirabayashi, Y., Kanae, S., Emori, S., Oki, T., Kimoto, M., 2008. Global projections of changing risks of floods and droughts in a changing climate. Hydrolog. Sci. J. 53 (4), 754–772.

Hirabayashi, Y., Döll, P., Kanae, S., 2010. Global-scale modeling of glacier mass balances for water resources assessments: Glacier mass changes between 1948 and 2006. J. Hydrol. 390, 245–256. http://dx.doi.org/10.1016/j.jhydrol.2010.07.001.

Hock, R., 1999. A distributed temperature-index ice- and snowmelt model including potential direct solar radiation. J. Glaciol. 45, 101–111.

Hock, R., Holmgren, B., 2005. A distributed surface energy-balance model for complex topography and its application to Storglaciären, Sweden. J. Glaciol. 51 (172), 25–36.

Hock, R., Radić, V., Woul, M.D., 2007. Climate sensitivity of Storglaciären, Sweden: an intercomparison of mass-balance models using ERA-40 re-analysis and regional climate model data. Ann. Glaciol. 46, 342–348.

Immerzeel, W.W., van Beek, L.P.H., Konz, M., Shrestha, A.B., Bierkens, M.F.P., 2012. Hydrological response to climate change in a glacierized catchment in the Himalayas. Clim. Change 110, 721–736. http://dx.doi.org/10.1007/s10584-011-0143-4.

Iwata, S., Aoki, T., Kadota, T., Seko, K., Yamaguchi, S., 2000. Morphological evolution of the debris cover on Khumbu Glacier, Nepal, between 1978 and 1995. In: Raymond, C.F., Nakawo, M., Fountain, A. (Eds.), Debris-Covered Glaciers. IAHS Publication, Wallingford, UK, Proceedings from a Workshop Held at Seattle, WA, USA, pp. 3–11.

Jarvis, A., Reuter, H.I., Nelson, A., Guevara, E., 2008. Hole-filled seamless SRTM data V4, International Centre for Tropical Agriculture (CIAT) <http://srtm.csi.cgiar.org/> (accessed: 12.03.11).

Kang, E., Cheng, G., Lan, Y., Jin, H., 1999. A model for simulating the response of runoff from the mountainous watersheds of inland river basins in the arid zone of northwest China to climatic changes. Sci. China Ser. D 42, 52–63.

Klok, E.J., Oerlemans, J., 2002. Model study of the spatial distribution of the energy and mass balance of Morteratschgletscher, Switzerland. J. Glaciol. 48 (163), 505–518.

Kondo, J. (Ed.), 1994. Meteorology of Water Environment. Asakura, Tokyo (In Japanese).

Lemke, P., Ren, J., Alley, R.B., Allison, I., Carrasco, J., Flato, G., Fujii, Y., Kaser, G., Mote, P., Thomas, R.H., Zhang, T., 2007. Observations: changes in snow, ice and frozen ground. In: Solomon, S., Qin, D., Manning, M., Chen, Z., Marquis, M., Averyt, K.B., Tignor, M., Miller, H.L. (Eds.), Climate Change 2007: The Physical Science Basis. Cambridge University Press, Cambridge, United Kingdom and New York, NY, USA, p. 356.

Li, J., Su, Z., 1996. Glaciers in the Hengduan Mountains. Science Press, Beijing (In Chinese, pp. 1–110).

Liu, S., Xie, Z., Su, Z., Song, G., Wang, N., 1994. Accumulation, ablation and ice formation of Hailuogou Glacier in the Gongga Mountain. In: Xie, Z.a.V.M.K. (Ed.), Glaciers and environment in the Qinhai-xizang (Tibet) Plateau (I) –The Gongga Mountain. Science Press, Beijing and New York, pp. 65–80.

Liu, S., Zhang, Y., Zhang, Y., Ding, Y., 2009. Estimation of glacier runoff and future trends in the Yangtze River source region. China. J. Glaciol. 55 (190), 353–362.

Liu, Q., Liu, S., Zhang, Y., Wang, X., Zhang, Y., Guo, W., Xu, J., 2010. Recent shrinkage and hydrological response of Hailuogou glacier, a monsoon temperate glacier on the east slope of Mount Gongga. China. J. Glaciol. 56 (196), 215–224.

Matsuda, Y., Fujita, K., Ageta, Y., Sakai, A., 2006. Estimation of atmospheric transmissivity of solar radiation from precipitation in the Himalayas and Tibetan Plateau. Ann. Glaciol. 43, 344–350.

Mattson, L.E., Gardner, J.S., Young, G.J., 1993. Ablation on debris covered glaciers: an example from the Rakhiot Glacier, Punjab, Himalaya. In: Young, G.J. (Eds.), Snow and Glacier Hydrology. IAHS Publication, Proceedings of the Kathmandu Symposium, November 1992, pp. 289–296.

Mihalcea, C. et al., 2006. Ice ablation and meteorological conditions on the debris-covered area of Baltoro glacier, Karakoram, Pakistan. Ann. Glaciol. 43, 292–300.

Mitchell, T.D., Jones, P.D., 2005. An improved method of constructing a database of monthly climate observations and associated high-resolution grids. Int. J. Climatol. 25, 693–712. http://dx.doi.org/10.1002/joc.1181.

Motoyama, H., 1990. Simulation of seasonal snowcover based on air temperature and precipitation. J. Appl. Meteorol. 29 (11), 1104–1110.

Nakawo, M., Young, G.J., 1981. Field experiments to determine the effect of a debris layer on ablation of glacier ice. Ann. Glaciol. 2, 85–91.

Nakawo, M., Young, G.J., 1982. Estimate of glacier ablation under a debris layer from surface temperature and meteorological variables. J. Glaciol. 28 (98), 29–34.

Nash, J.E., Sutcliffe, J.V., 1970. River flow forecasting through conceptual models. Part 1. A discussion of principles. J. Hydrol. 10 (3), 282–290.

Nicholson, L., Benn, D.I., 2006. Calculating ice melt beneath a debris layer using meteorological data. J. Glaciol. 52 (178), 463–470.

Oerlemans, J., Fortuin, J.P.F., 1992. Sensitivity of glaciers and small ice caps to greenhouse warming. Science 258, 115–117, doi:110.1126/science.1258.5079.1115.

Ohmura, A., 2001. Physical basis for the temperature-based melt-index method. J. Appl. Meteorol. 40, 753–761.

Ohmura, A., 2006. Changes in mountain glaciers and ice caps during the 20th century. Ann. Glaciol. 43, 361–368.

Østrem, G., 1959. Ice melting under a thin layer of moraine and the existence of ice cores in moraine ridges. Geogr. Ann. 41, 228–230.

Pu, J. (Ed.), 1994. Glacier Inventory of China VIII (The Changjiang River Drainage Basin). Gansu Culture Press, Lanzhou, pp. 117–129 (In Chinese).

Reichert, B.K., Bengtsson, L., Oerlemans, J., 2001. Midlatitude forcing mechanisms for glacier mass balance investigated using general circulation models. J. Climatol. 14, 3767–3784. http://dx.doi.org/10.1175/1520-0442(2001)3014<3767:MFMFGM>3762.3760.CO;3762.

Reid, T.D., Brock, B.W., 2010. An energy-balance model for debris-covered glaciers including heat conduction through the debris layer. J. Glaciol. 56 (199), 903–916.

Rignot, E., Rivera, A., Casassa, G., 2003. Contribution of the Patagonia Icefields of South America to sea level rise. Science 302, 434–437. http://dx.doi.org/10.1126/science.1087393.

Röhl, K., 2008. Characteristics and evolution of supraglacial ponds on debris-covered Tasman Glacier. New Zealand. J. Glaciol. 54 (188), 867–880.

Sakai, A., Fujita, K., 2010. Formation conditions of supraglacial lakes on debris-covered glaciers in the Himalaya. J. Glaciol. 56 (195), 177–181.

Sakai, A., Takeuchi, N., Fujita, K., Nakawo, M., 2000. Role of supraglacial ponds in the ablation processes of a debris-covered glacier in the Nepal Himalayas. In: Raymond, C.F., Nakawo, M., Fountain, A. (Eds.), Debris-Covered Glaciers. IAHS Publication, Wallingford, UK, Proceedings from a Workshop held at Seattle, WA, USA, pp. 119–130.

Sakai, A., Nakawo, M., Fujita, K., 2002. Distribution characteristics and energy balance of ice cliffs on debris-covered glaciers, Nepal Himalaya. AAAR 34 (1), 12–19.

Sakai, A., Fujita, K., Nakawo, M., Yao, T., 2009. Simplification of heat balance calculation and its application to the glacier runoff from the July 1st Glacier in northwest China since the 1930s. Hydrol. Process. 23 (4), 585–596. http://dx.doi.org/10.1002/hyp. 7187.

Scherler, D., Bookhagen, B., Strecker, M.R., 2011. Spatially variable response of Himalayan glaciers to climate change affected by debris cover. Nat. Geosci. 4, 156–159. http://dx.doi.org/10.1038/ngeo1068.

Shi, Y., Liu, S., 2000. Estimation on the response of glaciers in China to the global warming in the 21st century. Chinese Sci. Bull. 45, 668–672.

Su, Z., Liu, S., Wang, N., Shi, A., 1992. Recent fluctuations of glaciers in the Gongga Mountains. Ann. Glaciol. 16, 163–167.

Su, Z., Song, G., Cao, Z., 1996. Maritime characteristics of Hailuogou Glacier in the Gongga Mountains. J. Glaciol. Geocryol. 18, 51–59 (In Chinese with English abstract).

Yasunari, T.J., Koster, R.D., Lau, K.-M., Aoki, T., Sud, Y.C., Yamazaki, T., Motoyoshi, H., Kodama, Y., 2011. Influence of dust and black carbon on the snow albedo in the NASA Goddard Earth Observing System version 5 land surface model. J. Geophys. Res. 116, F03017. http://dx.doi.org/10.1029/2010JF001939.

Yatagai, A. et al., 2009. A 44-year daily gridded precipitation dataset for Asia based on a dense network of rain gauges. SOLA 5, 137–140. http://dx.doi.org/10.2151/sola.2009-035.

Zhang, Y., Fujita, K., Liu, S., Liu, Q., Wang, X., 2010. Multi-decadal ice velocity and elevation changes of a monsoonal maritime glacier, Hailuogou Glacier. China. J. Glaciol. 56 (195), 65–74.

Zhang, Y., Fujita, K., Liu, S., Liu, Q., Nuimura, T., 2011. Distribution of debris thickness and its effect on ice melt at Hailuogou Glacier, southeastern Tibetan Plateau, using in situ surveys and ASTER imagery. J. Glaciol. 57 (206), 1147–1157.